A direct numerical simulation investigation of the synthetic jet frequency effects on separation control of low-Re flow past an airfoil

A direct numerical simulation investigation of the synthetic jet frequency effects on separation control of low-Re flow past an airfoil

Wei Zhang and Ravi Samtaney

Articles you may be interested in
Numerical study of the S809 airfoil aerodynamic performance using a co-flow jet active control concept
J. Renewable Sustainable Energy **7**, 023131 (2015); 10.1063/1.4919013

Lift-drag and flow structures associated with the "clap and fling" motion
Phys. Fluids **26**, 071906 (2014); 10.1063/1.4890221

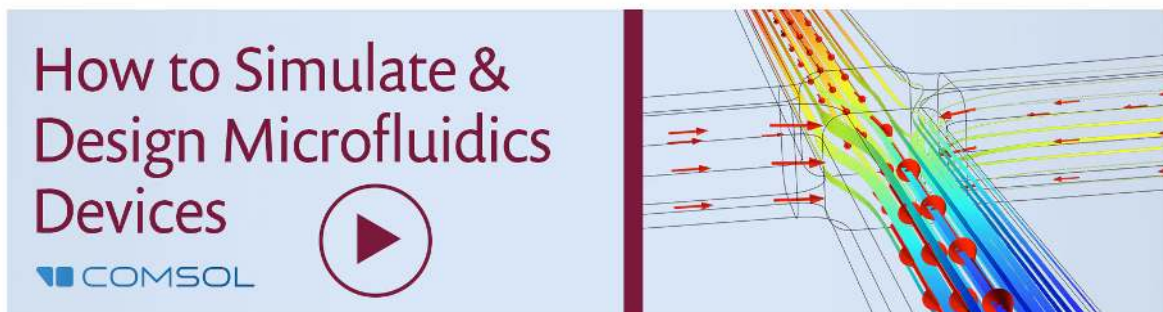A lift formula applied to low-Reynolds-number unsteady flows
Phys. Fluids **25**, 093605 (2013); 10.1063/1.4821520

A numerical study of the laminar necklace vortex system and its effect on the wake for a circular cylinder
Phys. Fluids **24**, 073602 (2012); 10.1063/1.4731291

Large-eddy simulations of a turbulent Coanda jet on a circulation control airfoil
Phys. Fluids **22**, 125105 (2010); 10.1063/1.3526757

A direct numerical simulation investigation of the synthetic jet frequency effects on separation control of low-Re flow past an airfoil

Wei Zhang and Ravi Samtaney
Mechanical Engineering, Physical Sciences and Engineering Division,
King Abdullah University of Science and Technology, 4700 KAUST, Thuwal,
23955-6900 Jeddah, Saudi Arabia

We present results of direct numerical simulations of a synthetic jet (SJ) based separation control of flow past a NACA-0018 (National Advisory Committee for Aeronautics) airfoil, at 10° angle of attack and Reynolds number 10^4 based on the airfoil chord length C and uniform inflow velocity U_0. The actuator of the SJ is modeled as a spanwise slot on the airfoil leeward surface and is placed just upstream of the leading edge separation position of the uncontrolled flow. The momentum coefficient of the SJ is chosen at a small value 2.13×10^{-4} normalized by that of the inflow. Three forcing frequencies are chosen for the present investigation: the low frequency (LF) $F^+ = f_e C/U_0 = 0.5$, the medium frequency (MF) $F^+ = 1.0$, and the high frequency (HF) $F^+ = 4.0$. We quantify the effects of forcing frequency for each case on the separation control and related vortex dynamics patterns. The simulations are performed using an energy conservative fourth-order parallel code. Numerical results reveal that the geometric variation introduced by the actuator has negligible effects on the mean flow field and the leading edge separation pattern; thus, the separation control effects are attributed to the SJ. The aerodynamic performances of the airfoil, characterized by lift and lift-to-drag ratio, are improved for all controlled cases, with the $F^+ = 1.0$ case being the optimal one. The flow in the shear layer close to the actuator is locked to the jet, while in the wake this lock-in is maintained for the MF case but suppressed by the increasing turbulent fluctuations in the LF and HF cases. The vortex evolution downstream of the actuator presents two modes depending on the frequency: the *vortex fragmentation and merging mode* in the LF case where the vortex formed due to the SJ breaks up into several vortices and the latter merge as convecting downstream; the *discrete vortices mode* in the HF case where discrete vortices form and convect downstream without any fragmentation and merging. In the MF case, the vortex dynamics is at a transition state between the two modes. The low frequency actuation has the highest momentum rate during the blowing phase and substantially affects the flow upstream of the actuator and triggers early transition to turbulence. In the LF case, the transverse velocity has a $1\%U_0$ pulsation at the position $18\%C$ upstream of the actuator. © *2015 AIP Publishing LLC.* [http://dx.doi.org/10.1063/1.4919599]

I. INTRODUCTION

Low Reynolds number flow ("low" here means $Re_C < 70\,000$[1] and $\sim 15\,000$ to $500\,000$[2]) around an isolated airfoil is relevant in the context of a variety of engineering applications such as the micro air vehicles, small wind turbines, and low-speed aircraft. Thanks to the advancement of modern technology and demands from such industries, smaller and lighter airfoils are urgently needed and are being developed and utilized in various engineering applications where low Reynolds number flows have to be dealt with.[3] Airfoils in such scenarios are often operated at high angle of attack (*AoA*) and thus suffer from flow separation due to an adverse pressure gradient (APG). At small angles of attack, the separated flow transitions to turbulent flow and reattaches to

27, 055101-1

the airfoil surface, forming the well known laminar separation bubble,[4] or simply does not reattach for stall or post-stall flow. In either of the above conditions, flow separation decreases the lift of the airfoil, and hence, flow separation control is an important goal.

Flow control techniques can be generally categorized as passive and active. Passive control devices (e.g., the vortex generator) have proved to be quite effective in delaying separation by producing vortices which exchange the momentum between the near wall region and the outer flow.[5,6] However, passive control strategies are typically not flexible for off-design conditions and permanently introduce a drag penalty, especially for low-*Re* flows. An active control device is generally implemented as a tiny hole of certain shape on the airfoil leeward surface. The hole is connected with a cavity (actuator) through which the fluid blowing or suction is conducted as a result of the piston stroke or pipe transportation of fluid from the other end. Active control is preferred over the passive one in that it is free of any device mounted on the airfoil surface, and is more flexible in adapting to various operating conditions by adjusting the magnitude and direction of the jet velocity. An active control device generally has three operating modes: steady blowing/suction, pulsed jet, and synthetic jet (SJ, also known as zero net mass flux jet or ZNMF jet). The steady blowing/suction mode[7–9] is the simplest in which the magnitude and direction of the jet velocity are held constant. Separation is alleviated through the mechanism of energizing the flow in the boundary layer, either by directly injecting high-momentum fluid through blowing or by introducing high-momentum fluid from the exterior cross-flow through suction. The pulsed jet[10–13] is similar to the steady blowing but differs in that the jet is injected into the boundary layer periodically. The boundary layer flow is sufficiently excited that perturbations amplify and transition to turbulence is initiated. In comparison with a steady blowing jet, a pulsed jet may penetrate deeper into the boundary layer with the same velocity. The SJ accommodates the features of the above two modes in the manner that periodic blowing and suction of fluid from the actuator are applied, and the mass flow rates of blowing and suction are equal in magnitude with a resulting zero net mass flux. The SJ is preferred over conventional steady blowing in that it could achieve the same prescribed performance improvement by a much smaller momentum coefficient, sometimes up to a saving of two orders of magnitude.[5] The actuator required could be small and light and is independent of the main propulsive system (see Glezer and Amitay[14] and references therein), which makes the SJ a competitive candidate in potential engineering applications.

The SJ-based separation control has been widely studied both numerically and experimentally for either an isolated airfoil or other types of configuration, as reviewed by Gad-el-Hak and Bushnell,[15] Greenblatt and Wygnanski,[5] Glezer and Amitay,[14] and Zhang *et al.*[16] Avdis *et al.*[17] performed a large-eddy simulation (LES) study on a turbulent boundary layer flow over a nominally 2D hump mounted on a flat plate at chord Reynolds number $Re_C \approx 9.4 \times 10^5$. The SJ resulted in an approximately 30% reduction of the time-averaged size of the separation zone, in reasonable agreement with the experimental value of 28%. Suzuki[18] performed a similar 2D simulation on a semi-circular cylinder at Reynolds number $Re_r = 4 \times 10^3$. He observed that the periodic forcing by the jet breaks the large-scale separated vortices into smaller ones, delaying the separation point and resulting in an improved aerodynamic performance. The experimental investigation by Naim *et al.*[19] concluded that, for flow over a circular cylinder, the control effects are not only determined by the position and forcing frequency of the jet but also by its direction with respect to the oncoming cross-flow. The SJ opposing the cross-flow is more effective in promoting transition at low momentum coefficient, thus reducing the laminar flow separation. Besides flow over bluff bodies, the SJ is also used for the separation control of flow in a diffuser-type configuration. Dandois *et al.*[20] conducted a LES study on turbulent boundary layer flow past a rounded ramp at $Re_h \approx 2.8 \times 10^4$ based on the step height. At low frequency (LF), the SJ decreases the maximum backflow velocity from 16% of the oncoming flow velocity down to 9%. The separation zone formed at the leeward side of the ramp is suppressed in the low frequency case but dramatically increases in the high frequency (HF) case. The numerical and experimental results in the literature examined above show that even for simple geometries, the effect of the SJ on the separation control is largely dependent on the parameters, such as the forcing frequency and the position of the actuator. Actuation with inappropriate parameters changes the control effects and may even lead to counterproductive outcomes.

Active separation control for flow over an airfoil is more complex than a cylinder or a ramp with respect to the determination and optimization of parameters. In the uncontrolled case, the flow is determined by the AoA of the airfoil and the chord Reynolds number Re_C; for compressible flow, it is also necessary to consider the Mach number Ma, the Prandtl number Pr, and the ratio of specific heat γ of the flow. The actuator of the SJ is characterized by its shape and dimensions, and its position on the leeward surface of the airfoil, normalized as $x^+ = x_{actuator}/C$. The key SJ forcing parameters include the velocity ratio u_{jet}/U_0 which is often normalized as the momentum coefficient C_μ, the reduced forcing frequency $F^+ = f_e C/U_0$, the profile of the velocity across the actuator exit, and the velocity direction with respect to the oncoming flow. These parameters form a multitude parameter space that is too large to be comprehensively investigated, either numerically or experimentally, to understand the flow physics and optimize the control effects. The SJ is normally implemented by fixing some of the parameters and changing the rest within certain regimes, and responses of the control effects are studied and correlated with the latter group. The parameters that substantially affect the separation control effects are the actuator location, the jet velocity direction, and the forcing frequency. For the actuator position, Amitay et al.[21] and Seifert and Pack[22] concluded that the actuator should be placed near the separation point of the uncontrolled case, while the experimental results of Buchmann et al.[23] show that an actuator at the leading edge is also effective. Raju et al.[24] performed 2D simulations for compressible flow past a NACA-4418 (National Advisory Committee for Aeronautics) airfoil at $Re_C = 4 \times 10^4$ and $AoA = 18°$, and their results show that the lift and lift-to-drag ratio may not be improved when the actuator is placed inside the separation zone, in agreement with the findings of Kotapati et al.[25] The jet velocity direction is determined by two angles: the pitch angle defined as the angle between the jet and the local wall, and the skew angle as the angle between projection of the jet on the wall and the cross-flow. Separation control is affected by the two angles through different mechanisms. The pitch angle determines the injection/suction of fluid into/from the boundary layer; a non-zero pitch angle induces spanwise vortices that energize the boundary layer flow by the entrainment effect of the cross-flow, and the virtual aero-shaping[26,27] may also take effect. A non-zero skew angle introduces extra streamwise vortices that enhance the mixing of flow inside and outside of the boundary layer. Along with the parameters regarding a single actuator, the control effects are also dependent on the shape of the actuator and the arrangement of the actuator array.[28–30]

The forcing frequency of the SJ is arguably the most important parameter and is indeed the key parameter to be optimized for better separation control effect.[24,31–33] Experimental and numerical results[31,34,35] reveal that the fundamental mechanism of separation control by a SJ is the formation of coherent roll-up lifting vortices not far from the airfoil surface. Such vortices are also observed in the cases of a nominally 2D hump[17] and flat plate.[13] The effectiveness of separation control depends on the receptivity of the mean flow to the imposed actuation. To achieve better performance, the SJ should be operated at an appropriate forcing frequency once the forcing amplitude (velocity ratio u_{jet}/U_0) is above a threshold value. Here, we give a brief description about the naturally occurring frequencies for flow over an airfoil that are important to determine the forcing frequency (for a more detailed exposition, the reader is encouraged to consult Refs. 31, 33, 36, and 37). At certain Reynolds number, there might be three natural frequencies depending on the AoA for flow over a thin airfoil. At a low AoA, the attached flow over the airfoil, although subjected to an APG, does not separate, and thus, the flow is dominated by the wake instability and is characterized by the frequency f_{wake}. As the AoA increases, the attached flow separates at a position close to the leading edge as a result of the APG, and the separated shear layer may reattach before the trailing edge. In this case, there are three natural frequencies: f_{SL}, f_{sep}, and f_{wake}, denoting the frequency of rolled-up vortices in the shear layer, the unsteady fluctuation in the separation bubble, and in the wake, respectively. At high AoA where separation is severe and post-stall flow dominants, the flow behaves like that pasts a bluff body and is characterized by f_{SL} and f_{wake}. Based on this classification, it is clear that the effective forcing frequency relies on the AoA and other flow parameters; thus, the determination of the effective or optimal frequency is case dependent and should be determined based on the uncontrolled flow physics. It is also noted here that this classification can be somewhat confusing in some studies owing to the fact that one or more frequencies are mistakenly represented by other types of frequencies.

Greenblatt and Wygnanski[5] comprehensively reviewed the separation control for flow over a post-stall airfoil using the SJ as well as other techniques. They summarized that for the majority of the selected cases, the optimal reduced frequency $F^+ = f_e X_{te}/U_0$ is in the range of $0.3 \leq F^+ \leq 4.0$, in which X_{te} is the distance from the actuator to the trailing edge. Wu $et\ al.$[31] performed 2D simulations on turbulent flow past a post-stall NACA-0012 airfoil at $Re_C = 5 \times 10^5$ and $AoA = 18° - 35°$. They found that the effective reduced frequency is in the range of $0.3-2.0 f_{wake}$ where the flow is resonant to the excitation in some form. At $AoA = 25°$, the lift-to-drag ratio increases 49.2% and 46.7% for $f_e/f_{wake} = 1.0$ and 2.0, respectively, at which harmonic resonance of vortex shedding occurs. The largest lift increase is 73.2% at the subharmonic resonance of vortex shedding $f_e/f_{wake} = 0.5$. Duvigneau and Visonneau[32] simulated the 2D flow over a NACA-0015 airfoil at $Re_C = 8.96 \times 10^5$ and $AoA = 12° - 24°$ and proposed an optimization procedure to maximize the lift at different $AoAs$ by modifying the velocity ratio, pitch angle, and forcing frequency of the SJ. The reduced frequency $F^+ = f_e C/U_0$ reaches its optimal value around 0.8 for $AoA = 14° - 20°$, while a much smaller value of 0.25 is found for $AoA = 22°$. They conclude that the optimal mean lift with regard to the whole variation range of AoA is obtained at $F^+ = 0.85$. You and Moin[38] conducted a LES study for the same airfoil and Reynolds number at $AoA = 16.6°$, in which the SJ gives a 70% lift increase when operated at $F^+ = 1.284$. The separation control for flow over a NACA-0015 airfoil is also experimentally studied by Tuck and Soria[39] and Buchmann $et\ al.$[23] at $Re_C = 3 \times 10^4$ and $AoA = 18°$. They found that the optimal forcing frequencies in terms of maximum lift are $F^+ = 0.65$ and $F^+ = 1.3$, which are the wake frequency f_{wake} and its harmonic $2 f_{wake}$. In the numerical simulation of Raju $et\ al.$[24] for a stalled NACA-4418 airfoil at $Re_C = 4 \times 10^4$ and $AoA = 18°$, a separation bubble is formed close to the leading edge and the uncontrolled flow is characterized by all three natural frequencies f_{SL}, f_{sep}, and f_{wake}. The results reveal that the SJ forcing near $f_{sep} \sim O(1)$ is effective in reducing the size of the separation bubble and increasing the lift-to-drag ratio, while the separation control is unfavorable when the reduced forcing frequency is higher $f_{SL} \sim O(10)$, at which the shear layer vortices merge into larger ones and separation becomes more severe. The phenomenon of ineffective forcing at high frequency due to the merging of Kelvin-Helmholtz vortices is also observed by Kotapati[33] for flow over a flat plate with an elliptic leading edge and a blunt trailing edge. However, an opposite conclusion was reached based on the experimental results of Amitay $et\ al.$[21] Their results show that there are two distinct regimes of the reduced frequency $F^+ = f_e C/U_0$ where enhancement of lift-to-pressure drag ratio L/D_p occurs: either when the forcing frequency is the same order as the shedding frequency f_{wake} ($F^+ \leq 4.0$) or it is more than an order of magnitude larger ($F^+ \geq 10.0$). This unusual variation may be attributed to the airfoil configuration and the scaling manner of the reduced frequency. For certain types of airfoils, the length scale C or X_{te} may be inappropriate, and the reduced frequency should be scaled by the separation bubble length.[5]

Compared with the naturally developing flow past an isolated airfoil in the uncontrolled state, the introduction of the SJ imposes a periodic excitation due to which the flow is largely determined. For a post-stall state, the leading edge separated shear layer has a rich spectrum that may respond to a variety of disturbances of different frequencies.[31] The separation pattern and the initial stages of the separated shear layer development are affected and may partially be locked to the forcing frequency or its harmonics, resulting a quasi-periodic flow whose unsteady behavior is determined by the coherent structures arising from the SJ. The wake has a weak dependency on the excitation of the SJ since it is relatively far from the actuator, and primarily because it is governed by its own global instability mechanism.[33] In the present study, we perform direct numerical simulations (DNSs) on the low-Re stalled flow past an isolated airfoil controlled by the SJ. The main objective is to investigate the frequency effects on the aerodynamic performance improvement and the dynamic characteristics of the coherent structures. Based on the high fidelity results from the DNS computations, the present investigation emphasizes flow resonance to the imposed periodic actuation, and the formation and evolution patterns of the near-field structures are also analyzed. Section II gives a detailed description about the physical problem and the numerical methods used in the simulation. Section III gives the simulation results, including the aerodynamic performance improvement, the flow resonance to the actuation, and the formation and evolution of the coherent structures. Some conclusions are presented in Sec. IV.
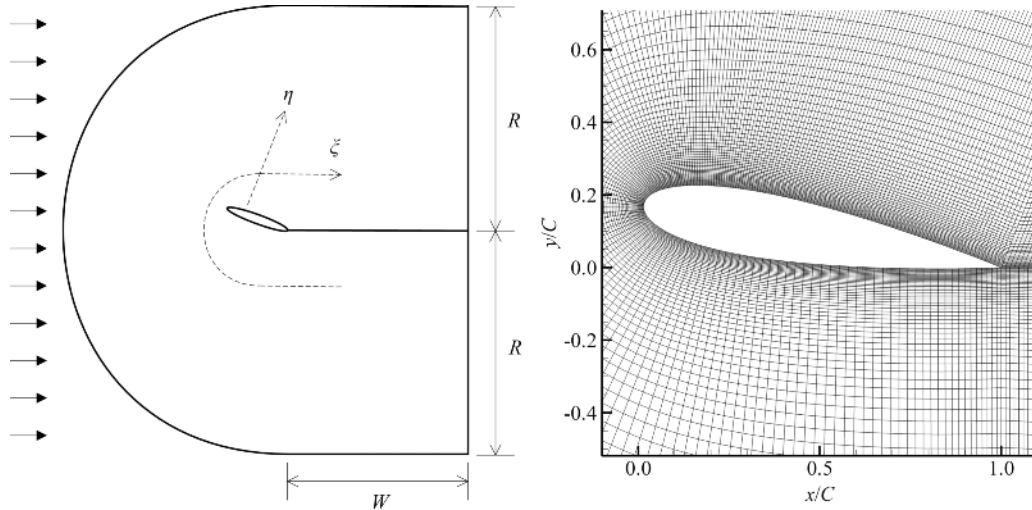
FIG. 1. Schematic illustration of the physical model and the mesh details close to the airfoil. The mesh is plotted every fifth gridline for clarity.

II. PHYSICAL MODEL, NUMERICAL METHOD, AND FLOW DIAGNOSTICS

A. Physical setup

The physical model of the present problem is shown in Figure 1. The NACA-0018 airfoil is rescaled to unit chord length C and is extended to include a sharp trailing edge located at $(x/C, y/C) = (1.0, 0.0)$. The airfoil is assumed to be straight in the spanwise direction. The angle of attack is 10°. The Reynolds number is $Re_C = 10^4$ based on the chord length C and the uniform inflow velocity U_0. The profile of the airfoil is not modified for the baseline (uncontrolled) case, while an actuator of the SJ is placed at the leeward surface close to the leading edge for the controlled cases.

The actuator of the SJ is modeled as a straight spanwise slot for the DNSs. The smoothly curved airfoil leeward surface is modified by the exit of the actuator, denoted by the straight dashed line in Figure 2. As a result, the surface curvature is discontinuous at the junctions between the actuator exit and the airfoil surface. In the present study, the SJ is simply modeled by the time-periodic velocity boundary conditions at the actuator exit,[11–13,18,24] instead of a cavity-type actuator where the jet is realized by the piston stroke in the cavity.[17,20,33,38] Although phase lag exists between the piston velocity and the jet velocity,[23] and the jet will undergo viscous dissipation, we mainly focus on the effects of jet on flow separation control and neglect the implementation details of a synthetic jet.

There are several geometric and operational parameters for the actuator and the SJ, including the position $x^+ = x_{actuator}/C$ and width $w^+ = width/C$ of the actuator, the reduced frequency of the time-varying jet $F^+ = f_e C/U_0$, where f_e is the actuation frequency, and the profile and direction of
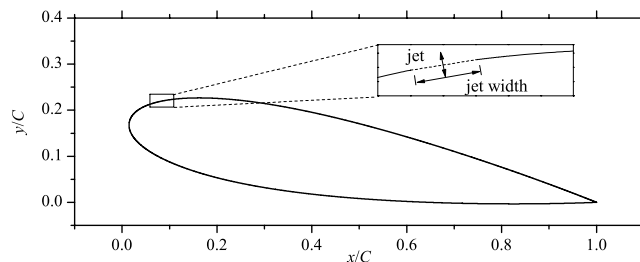

FIG. 2. Physical model of the synthetic jet.

the jet velocity. Due to the huge computational expense of each DNS computation, it is practically impossible to cover the whole parameter space. In the present study, we mainly focus on the effects of the frequency and choose fixed values for other parameters. The position of the actuator will be discussed in Sec. III. The width of the jet is $w^+ = 0.02$ and is resolved by 24 grid points. The direction of the jet is assumed to be normal to the local surface with zero spanwise component, and the velocity profile is of Poiseuille-type,

$$u_{\text{jet}}(r,t) = u_{\text{max}}[1 - (\frac{r}{\text{width}/2})^2]\sin(2\pi f_e t), \qquad -\text{width}/2 \leqslant r \leqslant \text{width}/2, \tag{1}$$

where the maximum velocity is fixed at $u_{\text{max}} = 0.2U_0$ and r is the distance to the jet center. The momentum coefficient is

$$C_\mu = \frac{\iiint \rho u_{\text{jet}}^2 dr\,dz\,dt}{\rho U_0^2 C L_z / f_e} = 2.13 \times 10^{-4}. \tag{2}$$

In the present study, the physical domain is discretized by a C-type mesh. The size of the computational domain should be large enough to minimize the influences of the artificially imposed boundary conditions. The domain size in the $x-y$ plane is determined by the wake length W (from the trailing edge to the outflow boundary) and the domain radius R (from the airfoil surface to the inflow boundary). Based on the DNS study by Jones $et\ al.$[40] for compressible flow past an airfoil at $Re_C = 5 \times 10^4$, a wake length of $W = 5C$ is deemed sufficient where a convective outflow condition is applied, and a domain radius of $R = 5.3C$ is enough to capture the outer potential flow. We fix the wake length and domain radius to be $10C$, i.e., the exterior boundary is at least $10C$ away from the nearest airfoil surface.

DNS requires that sufficiently large spanwise domain size to resolve the largest flow structure in this direction. In most DNS and LES studies at relatively higher Reynolds number, the spanwise domain size is normally chosen as $L_z = 0.1-0.2C$.[11,12,38,40] In the DNS study by Hoarau $et\ al.$[41] for incompressible flow past a NACA-0012 airfoil at $Re_C = 800$ and $20° AoA$, the dominant flow structure in the spanwise direction is about $0.64C$. In our DNS, we use a spanwise domain size of $L_z = C$, and its adequacy is confirmed by $a\ posteriori$ two-point correlation of the spanwise turbulent fluctuating velocity w', defined as[42]

$$r_{w'w'}(\Delta z) = \frac{\overline{w'(z,t)w'(z+\Delta z,t)}}{w'_{\text{rms}}(z)w'_{\text{rms}}(z+\Delta z)}, \tag{3}$$

where Δz is the spanwise separation distance, and the coefficient is averaged over combinations of probes with the same Δz. The variation of the coefficient with respect to Δz is plotted in Figure 3. Fröhlich $et\ al.$[43] concluded that the domain size is large enough if the velocity component in the periodic direction is uncorrelated within a separation distance of half the domain size. It is shown in Figure 3 that for the baseline simulation, the correlation coefficient decays to around zero for probes
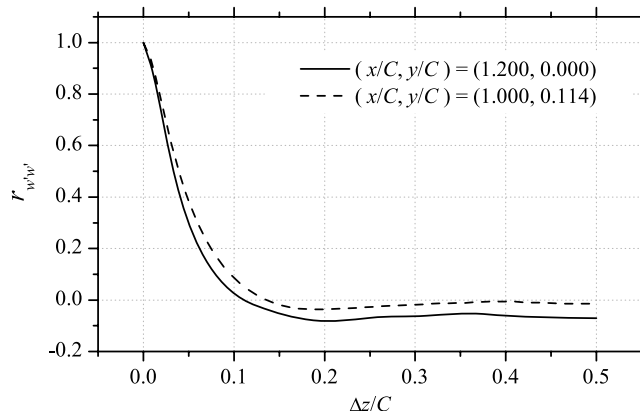

FIG. 3. Two-point correlation coefficient of w'-velocity between spanwise-oriented probes of the baseline case.

close to the trailing edge where turbulent flow has developed, confirming the adequacy of spanwise domain size.

The computational domain is discretized by a 2048×256 grid in the x–y plane with the grids clustered near the airfoil surface, and 128 equally spaced grids in the spanwise direction. During the entire time of all the simulations, the maximum $\Delta\eta^+$ is ≈ 0.6 and maximum $\Delta\xi^+$ and Δz^+ are ≈ 5.0 and ≈ 20.0, respectively. It is noted that the maximum Δz^+ (and also the maximum $\Delta\xi^+$ and $\Delta\eta^+$) appear close to the airfoil leading edge where the flow impinges on the wall and turns its direction to move along it. The flow in the vicinity of the leading edge is still laminar. The friction velocity is maximum in this region as a result of the large wall-tangent velocity. For flow close and downstream of the actuator ($x/C = 0.12 - 0.14$), the maximum Δz^+ on the upper surface rapidly drops to around 5.0. The other two components of mesh spacing, $\Delta\eta^+$ and $\Delta\xi^+$ also decrease further downstream. These values indicate that the resolution in the region of turbulent flow is adequate.

B. Solution method

The governing equations for the present simulations are the three-dimensional incompressible continuity equation and Navier-Stokes equations in non-dimensional form,

$$\frac{\partial u_k}{\partial x_k} = 0, \tag{4}$$

$$\frac{\partial u_i}{\partial t} + \frac{\partial u_k u_i}{\partial x_k} = -\frac{\partial p}{\partial x_i} + \frac{1}{Re_C}\frac{\partial^2 u_i}{\partial x_k \partial x_k}, \tag{5}$$

where $Re_C = U_0 C/\nu$ is the Reynolds number; $(u_1, u_2, u_3) \equiv (u, v, w)$ are the velocity components; p is the pressure; $(x_1, x_2, x_3) \equiv (x, y, z)$ are the Cartesian coordinates representing the streamwise, transverse and spanwise directions.

A uniform flow $(u, v, w) = (U_0, 0, 0)$ is imposed at the inflow boundary. At the outflow plane, the convective outflow condition $\partial\mathbf{u}/\partial t + U_B \partial\mathbf{u}/\partial x = 0$ is implemented, in which U_B is the bulk velocity. A no-slip boundary condition for velocity is prescribed on the airfoil surface except for the actuator where the velocity is applied in the form of Eq. (1). Periodic boundary condition is employed in the spanwise direction.

A generalized curvilinear coordinate transformation is applied from the physical domain (x, y, z) to the computational domain $(\xi_1, \xi_2, \xi_3) \equiv (\xi, \eta, z)$, in which the governing equations are spatially discretized on a collocated grid. The governing equations are spatially discretized by an energy conservative fourth-order scheme.[44] In order to minimize the aliasing error, the convective term is written and discretized in the skew-symmetric form.[44,45] The discretized governing equations are solved by a semi-implicit fractional step method.[46] The convective and viscous terms are explicitly and implicitly treated, respectively. The modified-Helmholtz equation resulting from the implicit treatment of viscous terms in the predictor step and the pressure Poisson equation are both solved using the multigrid solvers with point- and line-relaxed Gauss-Seidel smoothers. The time step size is about $2.0 \times 10^{-4} C/U_0$ in all simulations reported here, corresponding to a maximum CFL = 1.0. The initial condition is taken as one snapshot of the 2D simulation result, and the 3D simulation runs until time $70 C/U_0$ and then an additional $50 C/U_0$ for statistics.

C. Post-processing methods for flow diagnostics

Flow past a bluff body at low Reynolds number is predominantly determined by the time-dependent nature of the large-scale vortex shedding. As the Reynolds number increases, the flow is still dominated by the vortex shedding, but stochastic velocity and pressure fluctuations are observed. In order to better understand the evolution of the coherent structures, a triple-decomposition is applied to the velocity and pressure field data.[47] The flow past an airfoil manipulated by the natural vortex shedding or the SJ is written as

$$\phi(\mathbf{x}, t) = \overline{\phi}(\mathbf{x}) + \phi^*(\mathbf{x}, t) + \phi'(\mathbf{x}, t), \tag{6}$$

where $\phi(\mathbf{x},t)$ is the instantaneous variable; $\overline{\phi}(\mathbf{x})$ is the time-averaged mean; $\phi^*(\mathbf{x},t)$ is the coherent component due to the large-scale vortex shedding and/or the SJ; $\phi'(\mathbf{x},t)$ is the stochastic turbulent fluctuation. Each component on the RHS of Eq. (6) can be computed based on the instantaneous flow field,

$$\overline{\phi}(\mathbf{x}) = \frac{1}{t_1 - t_0} \int_{t_0}^{t_1} \phi(\mathbf{x},t)dt, \tag{7}$$

$$\phi^*(\mathbf{x},t) = \frac{1}{n} \sum_{i=0}^{n-1} \phi(\mathbf{x}, t + i \cdot T) - \overline{\phi}(\mathbf{x}), \tag{8}$$

$$\phi'(\mathbf{x},t) = \phi(\mathbf{x},t) - \phi^*(\mathbf{x},t) - \overline{\phi}(\mathbf{x}), \tag{9}$$

where $t_1 - t_0$ stands for the duration of the simulation, and T is the period of the large-scale vortex shedding or the jet pulsation. In experiments the value of T is normally determined from a reference pressure or velocity signal at some fixed point,[48,49] while in present simulations, it is computed and averaged through spectral analysis on the flow field at several probes. Since we mainly focus on the flow around the airfoil and in near wake and the flow is locked to the forcing in the controlled cases, phase jitter[50] is not of great concern and is omitted.[51,52] The first term on the RHS of Eq. (8) is the phase-average over a number of instantaneous flow fields of the same phase; thus, the turbulent fluctuation is erased. In the rest of this paper, we use the overbar $\overline{\phi}$ to denote time-averaging during the whole simulation. The quantities are averaged in the spanwise direction unless specified otherwise.

III. RESULTS AND DISCUSSION

The present study is primarily a DNS investigation of flow control using a SJ. Table I lists the selected cases to be analyzed. For the baseline (uncontrolled) case, the airfoil profile is kept at its original state and no actuator is installed. The second case is the zero-jet case, in which an actuator is implemented on the airfoil leeward surface but no blowing/suction is applied and hence is an examination of the changes affected by the geometrical modification of the airfoil surface. The remained three cases are the controlled cases where the SJ is operated at different frequencies $F^+ = 0.5$, 1.0, and 4.0. Holman et al.[53] investigated a SJ discharging into a quiescent flow and proposed a vortex pair formation criterion in the form $Re_{jet}/S^2 > 1$ for a quasi-2D SJ similar to the one considered in this study, where S is the Stokes number of the SJ. This criterion is proposed to ensure that the vortex pair formed during the blowing phase is not ingested back into the actuator in the suction phase. In our simulation, the value of Re_{jet}/S^2 is 2.71, 1.35, and 0.34 for the LF, MF, and HF cases, respectively. The high-frequency SJ does not satisfy the criterion. However, the SJ in this study interacts with a cross-flow rather than discharges into a quiescent flow; hence, the vortex pair formed by the SJ during the blowing phase is convected downstream by the cross-flow and is not necessarily ingested back into the actuator in the suction phase.

The location of the SJ actuator is determined based on the results of the baseline case. As discussed in Sec. I, it is generally confirmed that the SJ is effective and efficient when located close to the leading edge separation point, but so far there is no consensus on whether it should be implemented upstream or downstream of the separation point. Here, we follow the conclusion of Raju et al.[24] that the SJ is ineffective when located within the separation bubble, and place it

TABLE I. Summary of simulation cases.

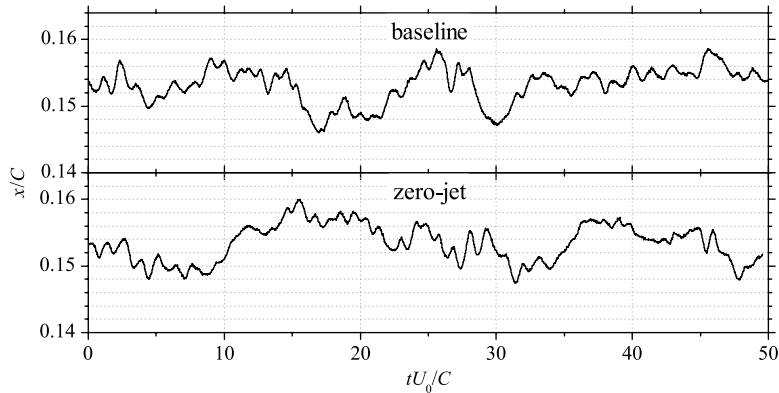| Case	Actuator	u_{max}/U_0	F^+	Note
1	No	...	...	Baseline
2	Yes	0.0	...	Zero-jet
3	Yes	0.2	0.5	LF jet
4	Yes	0.2	1.0	MF jet
5	Yes	0.2	4.0	HF jet

FIG. 4. Time history of the leading edge detachment position.

upstream of the most upstream location of the instantaneous separation point of the baseline case. Figure 4 presents the time histories of the leading edge separation position for the uncontrolled case. The attached flow separates at around $x/C = 0.15$ and the fluctuation of its position is limited to a small value of $\Delta x/C = 0.012$. Based on these results, the actuator of the SJ is positioned on the airfoil leeward surface with its centre located at $x^+ = 0.13$ for all the following simulations. The actuator exit is perpendicular to the local exterior normal direction of the original airfoil profile, and the windward and leeward locations of the actuator are at a distance of about $0.01C$ from its centre.

The introduction of the actuator and the SJ will affect the flow due to two distinct forcings: the geometric variation of the airfoil surface as a result of the actuator, and the forcing from the SJ. Although it is well-accepted that the latter contributes to the separation control, the installation of the actuator on the airfoil surface results in a slot (the actuator exit denoted by the dashed line in Figure 2) around which the surface curvature is not continuous. The discontinuities at the junctions between the actuator exit and the remaining smooth surface may trigger separation and affect subsequent flow development. Dandois et al.[20] performed a LES study on the SJ-based separation control for flow over a rounded ramp and investigated the effects of the actuator cavity by its presence without forcing. Their results show that the length of the separation bubble is $3.49h$ for the zero-jet case compared with $3.45h$ for the baseline case, where h is the ramp height. The mean streamwise velocity field shows only a slight difference between the two cases. The effects of the actuator geometry in the our airfoil configuration are presented from the following three aspects: flow separation location, mean flow, and aerodynamic forces. The position of the leading edge separation point is shown Figure 4; the maximum and minimum values in the zero-jet case are very close to those of the baseline case. The mean transverse velocity field is shown in Figure 5; it is clear that the passive existence of the SJ has almost negligible effects on the mean flow field. The mean force coefficients listed in Table II quantitatively confirm the negligible difference between the baseline and zero-jet cases, especially for the pressure distribution which is a dominant portion of the lift and drag. The tiny differences between the results of the baseline and zero-jet cases should
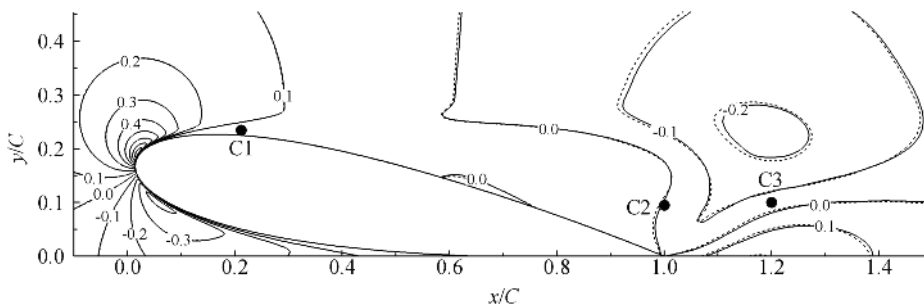

FIG. 5. Mean transverse velocity $\overline{v}/U_0$ of baseline case (solid line) and zero-jet case (dashed line).

TABLE II. Aerodynamic forces and related quantities.

Case	C_L	$(C'_L)_{rms}$	C_D	$(C'_D)_{rms}$	C_L/C_D	$\Delta C_L(\%)$	$\Delta(C_L/C_D)(\%)$
Baseline	0.2536	0.0465	0.1316	0.0062	1.9210	. . .	. . .
Zero-jet	0.2570	0.0495	0.1328	0.0070	1.9352	1.34	0.74
$F^+ = 0.5$	0.6974	0.1212	0.1259	0.0146	5.5393	175.00	188.36
$F^+ = 1.0$	0.7880	0.1126	0.1239	0.0129	6.3608	210.76	231.07
$F^+ = 4.0$	0.3660	0.0342	0.1091	0.0049	3.3547	44.32	74.08

mainly be attributed to the limitations of the simulations, including the resolution, the local mesh variation, and the time interval used for statistics. Based on these results, we conclude that the geometric variation brought by the actuator has negligible effects on the flow and that the control effects ought to be solely attributed to the periodic forcing of the SJ.

A. Mean flow characteristics

The implementation of the SJ for separation control is primarily intended to improve the aerodynamic performance of the airfoil. Table II lists the sectional force coefficients and related quantities. The force coefficients are defined as

$$C_L = \frac{\text{Lift}}{\frac{1}{2}\rho U_0^2 C L_z}, \quad C_D = \frac{\text{Drag}}{\frac{1}{2}\rho U_0^2 C L_z}, \tag{10}$$

in which $\rho = 1$ is the density of the fluid. The force coefficients are computed by integrating the pressure and shear stress over the airfoil surface. The introduction of SJ always improves the lift and lift-to-drag ratio although the drag is only slightly decreased. The reduced frequency $F^+ = 1.0$ is the optimum value, while the higher value $F^+ = 4.0$ also yields an improved aerodynamic performance. The fluctuations of the forces, indicated by their root-mean-square values, are augmented by the periodic forcing of the SJ. The augmentation is most remarkable for the LF case and rapidly decreases as the forcing frequency increases, and the force fluctuations for the HF case are approximately the same level as the baseline case. The dependence of the augmentation on the forcing frequency is mainly attributed to the different separation characteristics and evolution patterns of the coherent structures. For low-frequency actuation, the separation bubbles are generated during the blowing phase and are relatively stationary on the airfoil leeward surface, before convecting downstream during the suction phase and eventually leave the airfoil. The generation and convection of these separation bubbles drastically affect the local flow pattern close to the airfoil compared with those of the high-frequency actuation and results in the augmentation of the force coefficients. These flow patterns will be discussed in detail in Sec. III C.

We examine the mean streamwise velocity profiles for the baseline and controlled cases in Figure 6. Flow separation is evident upstream of $x/C = 0.20$ for all cases. For the baseline case, the
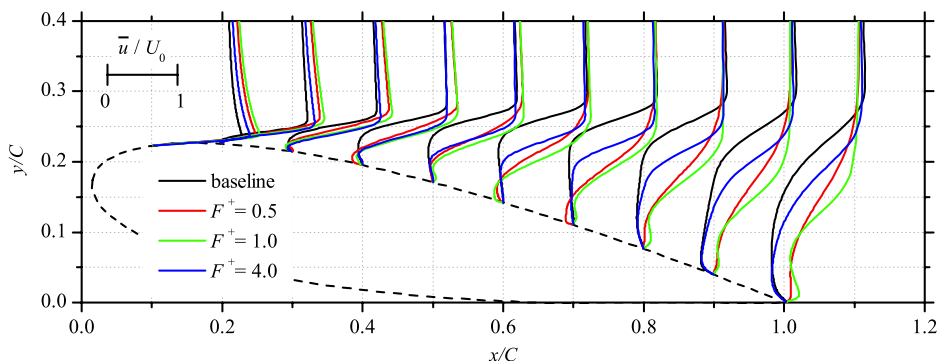
FIG. 6. Mean streamwise velocity profiles at equally spaced intervals $x/C = 0.1, 0.2, \ldots, 1.0$.

fluid flow in the separation zone has almost zero velocity over a major portion of its domain except the trailing edge region. The separation for the controlled cases is more intense in the sense that there is a maximum backflow velocity about $20\%U_0$ at $x/C = 0.30$ and 0.40, although the size of the separation bubble is relatively smaller along the y-direction. The effects due to the SJ control are more pronounced when the flow develops downstream and approaches the trailing edge. Starting from $x/C = 0.50$, the size of the separation bubble is smaller by at least 50% than that of the baseline case in the y-direction, and the backflow even disappears downstream of $x/C = 0.70$ and 0.80 for the MF and LF cases, respectively. For the HF case, the size of the bubble is only reduced by around 30% at the trailing edge. The velocity profile of the baseline case and the HF case is almost identical in the region close to the airfoil, normally within $0.05C$ away from the airfoil surface downstream of $x/C = 0.60$. This reflects that the SJ operated at high frequency is relatively less capable of affecting the flow close to the wall in the time-mean sense, with weak capability in separation control and smallest improvements in aerodynamic performance.

Figure 7 presents the pressure coefficient on both sides of the airfoil surface, and the skin friction coefficient on the leeward surface. The two coefficients are defined as

$$C_p = 2(p - p_{\text{ref}})/U_0^2, \tag{11}$$

$$C_f = \text{sgn}(u_s)\frac{1}{Re_C}(\frac{du_s}{d\mathbf{n}})_{\text{wall}}/U_0^2, \tag{12}$$

where p_{ref} is the reference pressure taken as the pressure at the outflow boundary $p_{\text{ref}} = 0$; u_s is the wall-tangent velocity; and $(du_s/d\mathbf{n})_{\text{wall}}$ is its wall-normal gradient on the wall. The skin friction coefficient is negative if the fluid moves from downstream to upstream direction, indicative of separation. There is a favourable pressure gradient over almost the entire lower surface of the airfoil. On the upper surface, there is a suction peak near the leading edge due to the acceleration of the flow followed by an immediate pressure recovery. The size of the separation zone is indicated by the pressure plateau, which is a large one for the baseline and HF cases and two smaller ones for the LF and MF cases. The introduction of the SJ substantially lowers (respectively, increases) the pressure on a major portion of the upper (respectively, lower) surfaces of the airfoil, which significantly improves the pressure lift. The high levels of C_f close to the leading edge result from the flow acceleration. In the separation region, C_f is close to zero for the baseline case except near the trailing edge since the flow is almost stationary in the separation zone as reflected in Figure 6. For the LF and MF cases, there are two regions with negative peak of C_f with a much smaller value than the baseline and HF cases, indicating the small but intensive separation bubbles induced by the SJ. The negative peaks are not precisely associated with the pressure plateaus due to the recirculation bubbles formed beneath the separation bubbles. The inset of the C_f figure presents the variation of C_f in the neighborhood region of the actuator. Compared with the baseline case, the SJ gives rise to the wall-tangent velocity (i.e., C_f is increased) and delays the leading edge separation. However, the HF actuation, although with the largest C_f improvement, does not produce small separation zone and the best aerodynamic performance improvements.
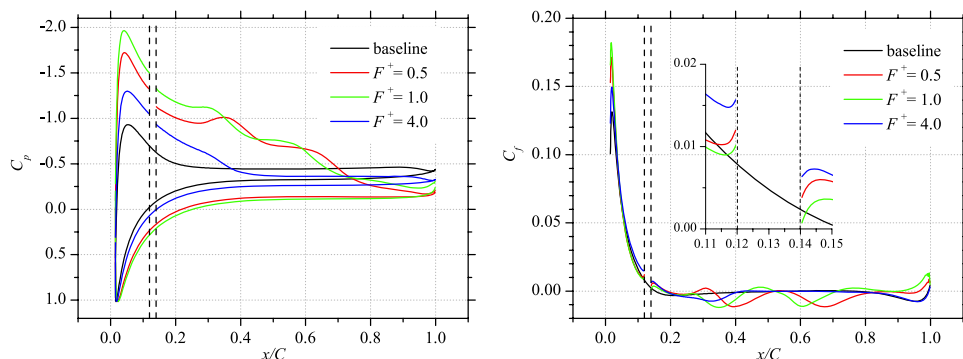

FIG. 7. Mean pressure coefficient and skin friction coefficient distributions. The vertical dashed lines denote the position of the actuator.

Based on the DNS results, it is concluded that the employment of the SJ significantly reduces the flow separation on the airfoil leeward surface; thus, the aerodynamic performance of the airfoil is substantially improved. The SJ operated at medium frequency (MF) $F^+ = 1.0$ is the optimal among the three frequencies, which gives the largest improvements to the lift and lift-to-drag ratio.

B. Flow resonance

1. Power spectra analysis

The dynamic response of the flow to the SJ provides insights into the vortex dynamics. The response of the flow to the forcing of the SJ is examined by the temporal variations of velocity at three probes above the airfoil leeward surface and in the near wake. The positions of the probes are shown in Figure 5. Probe C1 is located in the shear layer just downstream of the actuator of the SJ where separation occurs for the baseline case and where the SJ-induced vortex forms and rolls up for the controlled cases. Probe C2, located above the airfoil trailing edge, is inside the separation zone for the baseline and HF cases and in the cross-flow for the LF and MF cases. Probe C3 is located downstream of C2 where the separated vortices roll up and develop downstream and interact with the counterclockwise rotating vortices formed on the airfoil lower surface. The power spectra of the temporal variation of the transverse velocity v/U_0 at the three probes are given in Figure 8, and their major characteristics are summarized in Table III.

For the baseline case, the shear layer (probe C1) exhibits a broadband spectrum that could potentially respond to disturbances within a wide frequency range. Probes C2 and C3 in the separation zone and wake, respectively, also have relatively broadband spectra but dominant frequencies due to the wake instability are visible. The dominant natural frequency is not a regular sharp-peak in the spectrum but is a range of finite width, which is around $fC/U_0 = 1.0 \pm 0.2$ in the present case. For the LF case, the flow field is regularized by the SJ and becomes quasi-periodic, as shown by the harmonics of the spectra at the three probes. The flow in the shear layer does not respond to the forcing frequency of the SJ but rather to its second harmonic. At probe C2, the flow distinctly responds to the SJ (f_e) and its two harmonics ($2f_e$ and $3f_e$), while the higher harmonics are indistinguishable in the broadband spectrum as a result of the growing turbulence. The spectrum at probe
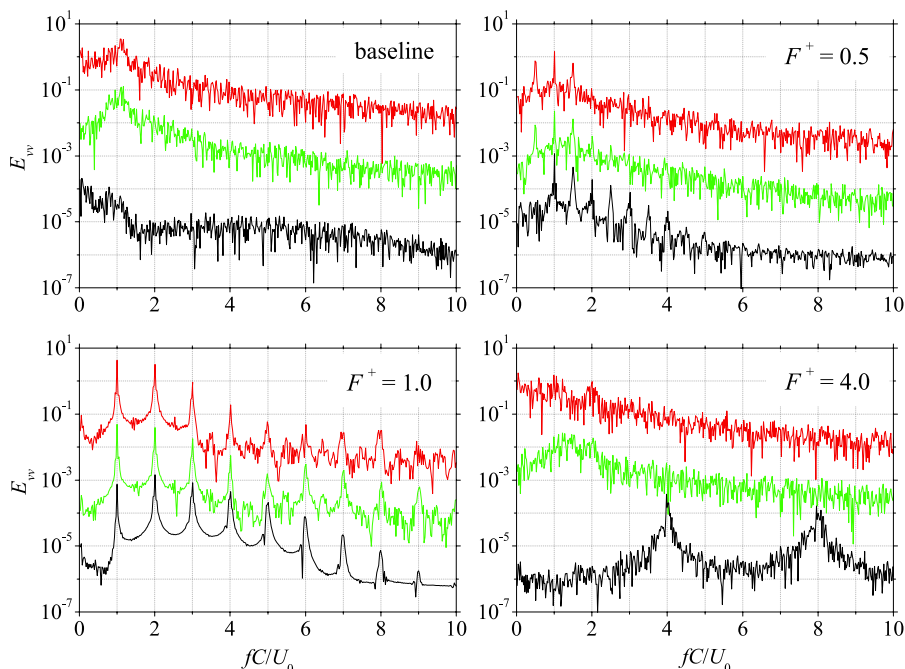

FIG. 8. Temporal power spectra of spanwise-averaged transverse velocity v/U_0 at the probes indicated in Figure 5. Black, red, and green lines, respectively, denote the probes C1, C2, and C3. The spectra are artificially separated for clarity.

TABLE III. Characteristics of the power spectra of velocity measured at the probes C1, C2, and C3 (Figure 5). f_e is the forcing frequency controlling the jet velocity in Eq. (1).

Case	Probe	Characteristic features
Baseline	C1	Broadband spectrum with no favorable resonant frequency.
	C2/C3	Broadband spectrum peaks near f_{wake} with notable turbulent fluctuations.
$F^+ = 0.5$	C1	Periodic about $2f_e$ with clear harmonics up to $8f_e$.
	C2/C3	Broadband spectrum, quasi-periodic about f_e with clear harmonics up to $3f_e$.
$F^+ = 1.0$	C1	Perfectly periodic about f_e. Well organized periodic vortical structures.
	C2/C3	Periodic about f_e with increasing turbulent fluctuations.
$F^+ = 4.0$	C1	Periodic about f_e with noticeable turbulent fluctuations.
	C2/C3	Broadband spectrum with no favorable resonant frequency.

C3 in the wake is similar except that the flow clearly responds to even higher harmonics ($4f_e$ and $5f_e$). The flow is locked to the forcing of the SJ for the MF case. The spectrum for probe C1 in the shear layer clearly consists of the fundamental frequency of the SJ excitation and its harmonics up to $9f_e$, representing a well organized vortical flow downstream of the actuator whose formation and unsteady development are almost perfectly periodic about the frequency f_e. The temporal variations of the flow at probes C2 and C3 show similar behavior that the flow is perfectly locked to the forcing of the SJ near and downstream of the trailing edge; thus, the turbulent fluctuations are weak. For the HF case where the jet is pulsating at a high frequency, the flow in the shear layer is locked to the forcing, while the spectra at the other two probes are broadband similar to those observed for the baseline case.

It is summarized here that the flow in the shear layer close to the actuator of the SJ has a broadband spectrum that responds to actuation at different frequencies ($F^+ = 0.5$, 1.0, and 4.0), and the flow is relatively well organized in that the formation and evolution of vortices are periodic to a certain degree. In regions close to the trailing edge and in the near wake, the spectra become broadband and the amplitudes of the harmonics are reduced due to the growing stochastic turbulent fluctuations. However, the application of the SJ at the frequency closest to the natural frequency of the uncontrolled flow (i.e., $F^+ = 1.0$) leads to the best locking of flow field to the excitation both in the shear layer and in the near wake region; thus, the flow is periodic even in the wake and the high-frequency turbulent fluctuations are suppressed.

2. Lock-in of flow to the SJ

Figure 9 shows the mean turbulent kinetic energy (T.K.E.) distributions to illustrate the growing turbulent fluctuations as the flow develops downstream. The u'-based T.K.E. is defined as $\overline{(u'u' + v'v' + w'w')}/(2U_0^2)$. For the baseline case, transition takes place in the separated shear layer and the flow is fully developed downstream of the trailing edge. The low-frequency actuation triggers earlier transition that occurs more close to the airfoil, while the turbulence intensity decreases
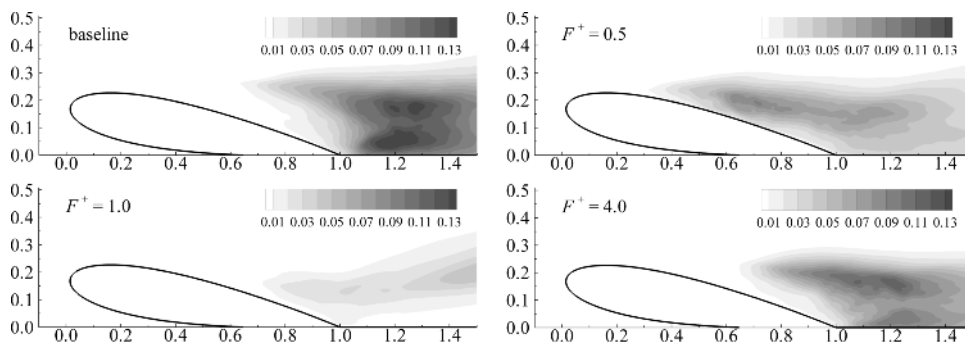

FIG. 9. Mean turbulent kinetic energy distributions in a neighborhood of the airfoil.

in the MF case. Since the high-frequency actuation only regularizes the near-field flow, the wake flow in the HF case is relatively fully developed to turbulence somewhat similar to the baseline case.

The flow dynamics may be further examined through a deterministic analysis of its response to the forcing of the SJ. The periodicity of the flow subjected to periodic forcing is investigated by a two-time correlation of the transverse velocity in the whole flow field. The two-time correlation coefficient is defined as[54]

$$C_v(x,y) = \frac{\overline{v(x,y,t) \cdot v(x,y,t+T)}}{\sqrt{\overline{v^2(x,y,t)}}\sqrt{\overline{v^2(x,y,t+T)}}},$$ (13)

where v is the instantaneous transverse velocity averaged in the spanwise direction. T is the normalized period of the pulsating flow field; in controlled cases it is chosen as the period of the forcing frequency ($T = 1/F^+$), while for the baseline case we use $T = U_0/(C f_{wake}) = 0.858$. In regions where the coefficient is one, the flow is steady or T-periodic and is fully deterministic to the periodic forcing of the SJ, while decorrelation and imperfect lock-in are indicated by smaller values of C_v. Lamballais et al.[54] suggested computing this correlation using a number of discrete snapshots within only two consecutive cycles to prevent false artificial correlation or decorrelation. In our simulations, the statistics lasts for at least 25 cycles (the LF case); the unsteady flow field cannot be perfectly T-periodic due to the turbulence fluctuations and phase jitter.[50] For a statistically time-invariant representation of the flow field, the coefficient is computed within as many as integer cycles in our study. The C_v distributions are shown in Figure 10. For the baseline case, decorrelation ($C_v < 1$) is pronounced downstream of the middle of the airfoil since transition to turbulent flow starts. Good correlation is observed close to the leeward surface for $x/C \in [0.8, 1.0]$. The backflow is quasi-steady in this region and is less affected by the cross-flow and wake vortices, and a similar trend is also observed in the HF case. Compared with the baseline case, the unsteady flow fields in the controlled cases are more or less locked to the periodic forcing and are more deterministic. The flow field is well correlated above the leeward surface and the decorrelation is only severe downstream of the trailing edge. For the MF case, it is seen that the whole flow field is almost perfectly locked to the periodic forcing of the SJ such that good correlation is observed even in the near wake. This deterministic analysis confirms the frequency dependent receptivity of the excitation of the separated flow. The separated shear layer and the wake can shift and lock to the excitation frequency and its harmonics, and this lock-in is pronounced when the forcing frequency is close to that of the uncontrolled flow, similar to the conclusions of Wu et al.[31]

C. Coherent structures

1. Vortex dynamics

The velocity and pressure of the flow can be decomposed into the time-averaged mean, the coherent, and the incoherent components as shown in Eq. (6). For the baseline case, the coherent component is primarily due to the large-scale vortex shedding that naturally develops as a result of
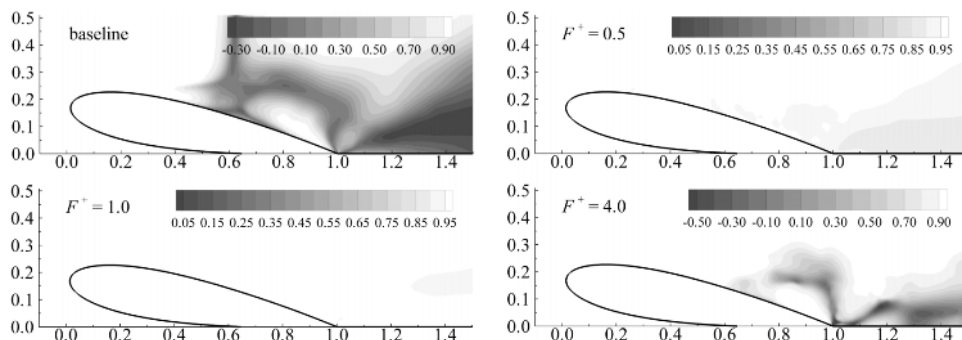

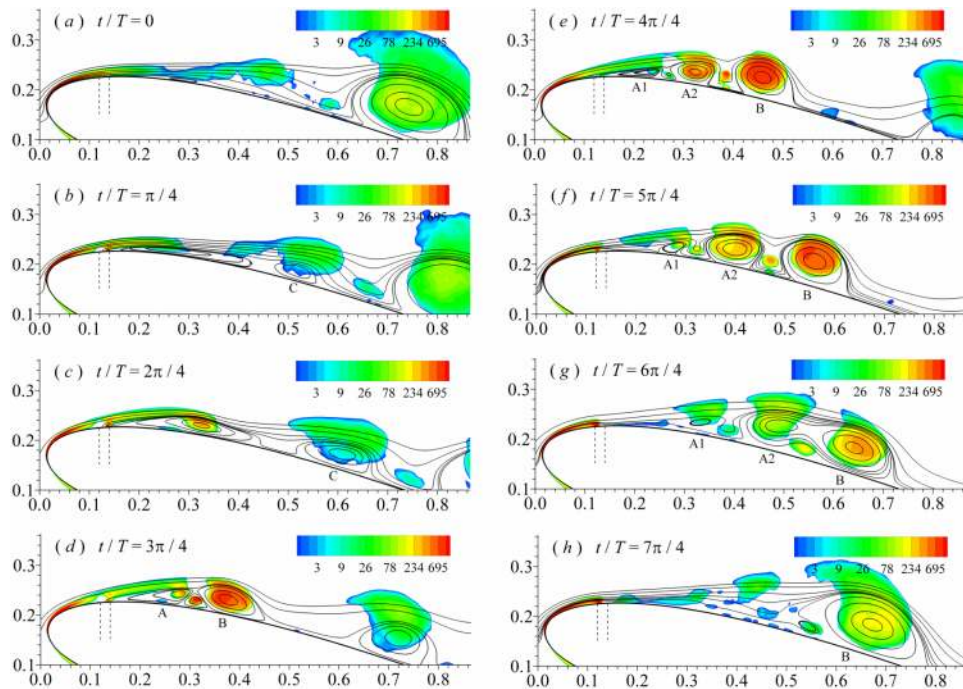FIG. 10. Frequency effect on the two-time correlation coefficient C_v.

FIG. 11. Evolutions of phase-averaged streamlines and the Q-invariant for the $F^+ = 0.5$ case. The vertical dashed lines denote the position of the actuator. The Q-field is plotted for [1, 1000] with 20 exponentially scaled levels. (a) $t/T = 0$; (b) $t/T = \pi/4$; (c) $t/T = 2\pi/4$; (d) $t/T = 3\pi/4$; (e) $t/T = 4\pi/4$; (f) $t/T = 5\pi/4$; (g) $t/T = 6\pi/4$; (h) $t/T = 7\pi/4$.

the flow instability, and the incoherent component is due to turbulent fluctuations. For the controlled cases, the periodic forcing exerted by the SJ determines the coherent structures of the flow and is important in flow separation and the evolution of vortices. In order to gain a better understanding about the time-dependent effects of the SJ on the flow, Figures 11-13 show the temporal evolution of the phase-averaged streamlines and $Q = -0.5u_{i,j}u_{j,i}$ at eight equally spaced time instants within one period for all three controlled cases. The forcing of the SJ consists of the blowing phase from $t/T = 0$ to $t/T = 4\pi/4$ and the suction phase from $t/T = 4\pi/4$ to $t/T = 8\pi/4(= 0)$.

For the LF case shown in Figure 11, the non-dimensional period of the forcing is the largest among all three controlled cases. The injection of fluid to the cross-flow produces a separation bubble just downstream of the actuator. The separation bubble first emerges around $x/C = 0.3$ at $t/T = 0$, which originates in the suction phase as a result of the roll up of the near wall vortex (A1 in (g)). The jet velocity increases until $t/T = 2\pi/4$ and the separation bubble increases in size in both the wall-tangent and wall-normal directions. The vortex is energized by the jet on the side close to the actuator, while the other side is less resistant to the high kinetic energy cross-flow and breaks up into two vortices, and the downstream one (vortex C in (b)) is convected away with the cross-flow. At $t/T = 3\pi/4$, the jet velocity is smaller compared with its peak value and the vortex close to the actuator breaks up into two vortices A and B. The vortex A further breaks up and three vortices appear (A1, A2, and B), as seen in (f). The three vortices are larger during the suction phase than the blowing phase during which they convect downstream along with the cross-flow. The vortices A2 and B merge into one single vortex, and A1 is remarkably weakened and finally vanishes at $t/T = 7\pi/4$.

The vortex dynamics in the MF case shown in Figure 12 is somewhat similar to the LF case but with some differences due to the higher frequency (smaller period) of the SJ actuation. First, the separation bubble emerges completely within the blowing phase, as seen in (b). The separation bubble grows but is much smaller than the one in the LF case in both wall-tangent and wall-normal directions. The smaller size is mainly due to the shorter duration of the blowing phase so that the growth of the bubble is less promoted by the virtual aero-shaping effect provided by the SJ. The second difference is that there is only one vortex breakup during the whole cycle, which is shown at
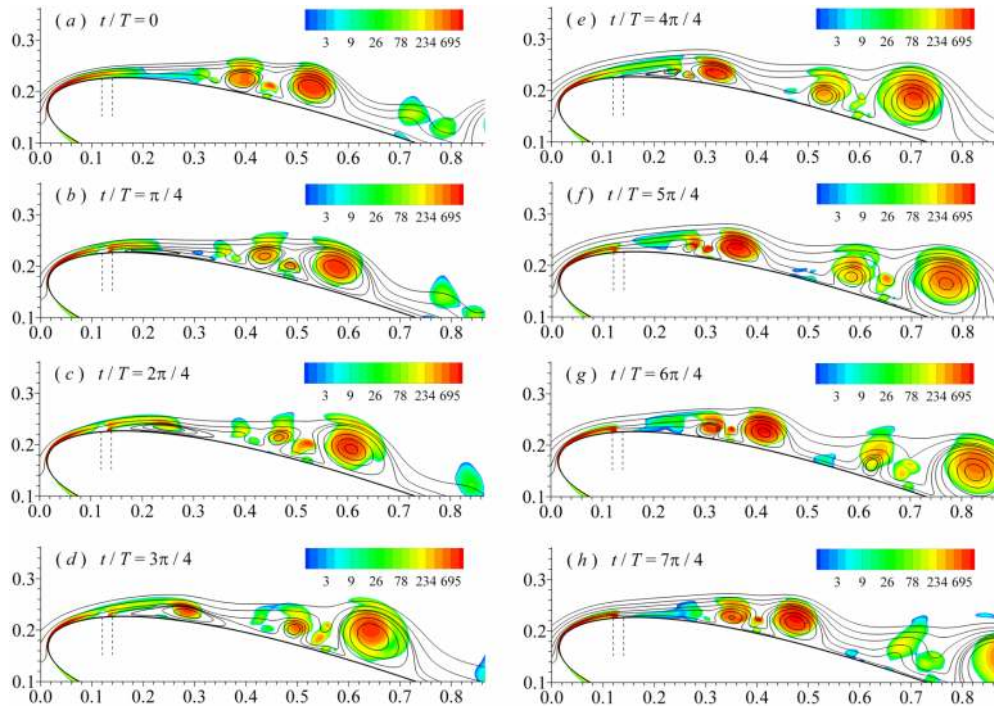
FIG. 12. Evolutions of phase-averaged streamlines and the Q-invariant for the $F^+ = 1.0$ case. The vertical dashed lines denote the position of the actuator. The Q-field is plotted for [1, 1000] with 20 exponentially scaled levels. (a) $t/T = 0$; (b) $t/T = \pi/4$; (c) $t/T = 2\pi/4$; (d) $t/T = 3\pi/4$; (e) $t/T = 4\pi/4$; (f) $t/T = 5\pi/4$; (g) $t/T = 6\pi/4$; (h) $t/T = 7\pi/4$.

FIG. 13. Evolutions of phase-averaged streamlines and the Q-invariant for the $F^+ = 4.0$ case. The vertical dashed lines denote the position of the actuator. The Q-field is plotted for [1, 1000] with 20 exponentially scaled levels. (a) $t/T = 0$; (b) $t/T = \pi/4$; (c) $t/T = 2\pi/4$; (d) $t/T = 3\pi/4$; (e) $t/T = 4\pi/4$; (f) $t/T = 5\pi/4$; (g) $t/T = 6\pi/4$; (h) $t/T = 7\pi/4$.
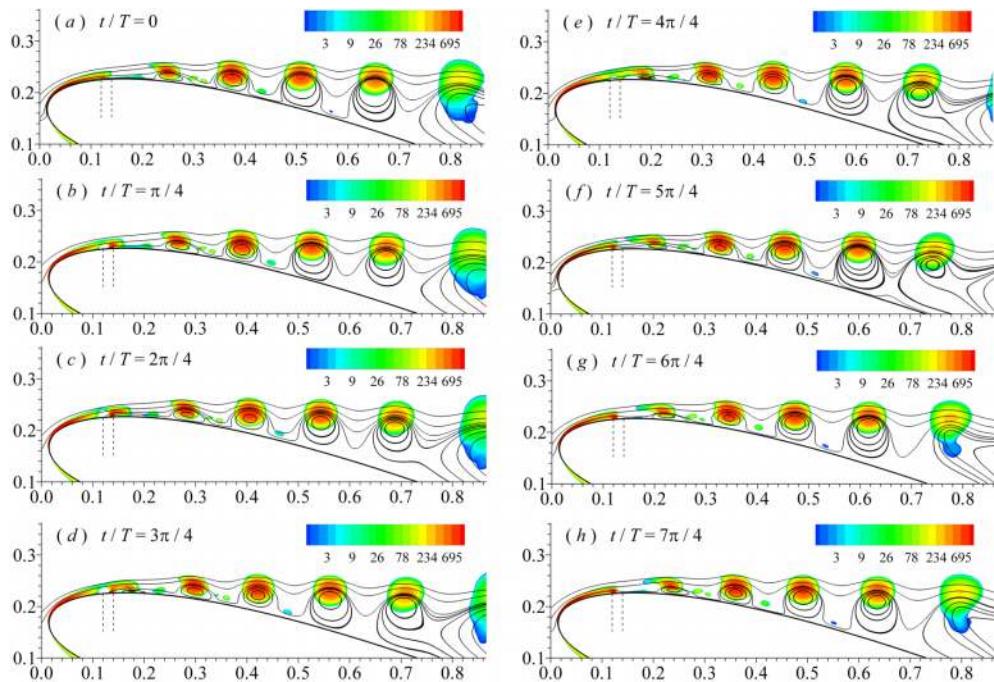
the end of the blowing phase $t/T = 4\pi/4$. The two smaller vortices develop downstream to form two individual ones and no merging is observed within the current streamwise scope.

The vortex dynamics in the HF case has a complete different scenario compared with its LF and MF counterparts, as shown in Figure 13. In the blowing phase, a small separation bubble forms quite close to the actuator. The pulsating frequency of the SJ is so high that the separation bubble is only slightly energized and is relatively smaller than those in the LF and MF cases. There is no vortex fragmentation and merging during the whole cycle. The rapidly pulsating forcing from the SJ generates a set of vortices; the vortices are energized primarily by the cross-flow and grow as they convect downstream.

From the above observations, we basically identify two modes of vortex dynamics depending on the forcing frequency of the SJ: the *vortex fragmentation and merging mode* and the *discrete vortices mode*. In the first mode that is observed in the LF case, the pulsating period of the SJ is long that a separation bubble grows mainly during the blowing phase. The separation bubble is large in the wall-tangent direction and is less resistant to the high kinetic energy cross-flow and breaks up into two individual vortices. This kind of fragmentation may take place more than once within one cycle. The individual vortices may merge as they develop downstream. In the second mode, observed in the HF case, the separation bubble emerging in the blowing phase is smaller in size especially in the streamwise direction. It develops downstream without any breakup and merging, forming a clear set of vortices. Based on this classification, we can find that the vortex dynamics in the MF case is a transition state between the above two modes.

2. Downstream convection of vortices

The evolution of the multiple vortices along the airfoil leeward surface, from the leading edge to the trailing edge, is depicted by the space-time diagrams of the instantaneous spanwise-averaged skin friction coefficient in Figure 14. Four cycles are presented for each controlled case. The fragmentation and merging of vortices are in accordance with the findings in Figures 11-13. The clockwise rotating vortices result in negative C_f. In the LF and MF cases, the separated vortices give large negative values of C_f, reflecting their high intensity compared with those in the HF case. This figure can be used to quantify the convection velocity of the discrete vortices obtained by computing the slopes of the stripes. In the present study, the convection velocity of the vortices in the LF and MF cases are $0.33U_0$ and $0.37U_0$, respectively, while a much larger value of $0.50U_0$ is observed in the HF case. Dandois et al.[20] comprehensively summarized the convection velocity of the shear layer vortices for flows with different configurations. The results show that the convection velocity is 0.5–$0.6U_0$ for most studies of flow over a backward facing step or a ramp, where the discrete vortices mode is observed downstream of the actuator.[20,17] The higher convection velocity in the HF case is similar to the convection velocity of two-dimensional Kelvin-Helmholtz vortical structures as discussed in the above studies since they exhibit similar discrete vortices mode. For the LF and
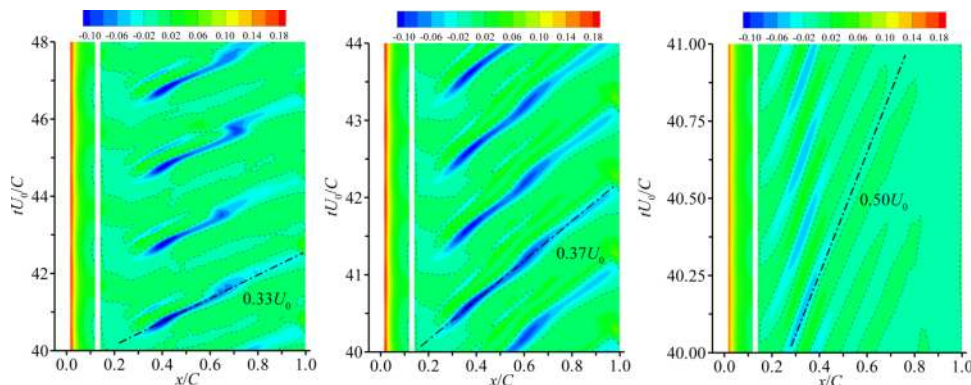

FIG. 14. Space-time diagrams of instantaneous spanwise-averaged skin friction coefficient C_f. From left to right: $F^+ = 0.5$, 1.0, and 4.0. The dashed line denotes the isoline $C_f = 0$. The actuator is denoted by the white zone.

MF cases, the virtual aero-shaping effect of the SJ[27] substantially modifies the profile of the airfoil during the blowing phase and the separated vortices formed downstream of the actuator are less affected by the cross-flow; the vortex downstream of the SJ shown in Figures 11(b) and 11(c) is elongated along the airfoil and hardly moves downstream. During the suction phase, there is no virtual aero-shaping and the elongated vortex breaks up into smaller ones which convect downstream with the cross-flow (see Figures 11(b)-11(d)). This stationary-convection pattern results in a small convection velocity in the LF and MF cases.

3. Coherent structures close to the SJ

The frequency effects of the SJ on the near-field coherent structures are quantitatively presented by the profiles of mean coherent Reynolds stresses in Figure 15. The profile at $x/C = 0.13$ is located at the centre of the actuator exit, while the profiles at $x/C = 0.12$ and $x/C = 0.14$ are positioned close to the edges of the actuator exit. The Reynolds stresses in the baseline case are almost zero ($< 10^{-5}$) within the range the profiles are presented ($0.11 \leq x/C \leq 0.40$) due to the quasi-stationary separated flow in this region. For the controlled cases, the extrema values of the Reynolds stresses occur at a short distance from the airfoil surface due to the inertia of the jet flow, with the exception of $\overline{v^*v^*}$ at the centre of the actuator exit where the maximum value is expected. A careful inspection reveals that the wall-normal location of the maximum stresses, in terms of y/C, is frequency dependent. The position is furthest from the surface for the LF case, while it is moving close to the surface as the frequency increases for the MF and HF cases owing to the smaller momentum of the jet added to the ambient cross-flow, or the smaller "stroke" length of the jet at higher frequency.[14] The magnitudes of the stresses also monotonically decrease with the frequency in the neighborhood of the actuator ($0.11 \leq x/C \leq 0.17$); the stresses are substantially suppressed by the high frequency fluctuation of the SJ, and the component $\overline{u^*u^*}$ is more affected that its value is only slightly larger than that of the baseline case. In the downstream region away from the actuator ($x/C \geq 0.20$), separated vortices form and their fragmentation and merging may occur, so that the stresses are less frequency dependent and depict different profiles compared with those upstream. As we have demonstrated in Figures 11-14, the momentum of jet flow and the intensity of the separated vortex in the LF case are the most pronounced among the controlled cases; thus, $\overline{u^*u^*}$ of
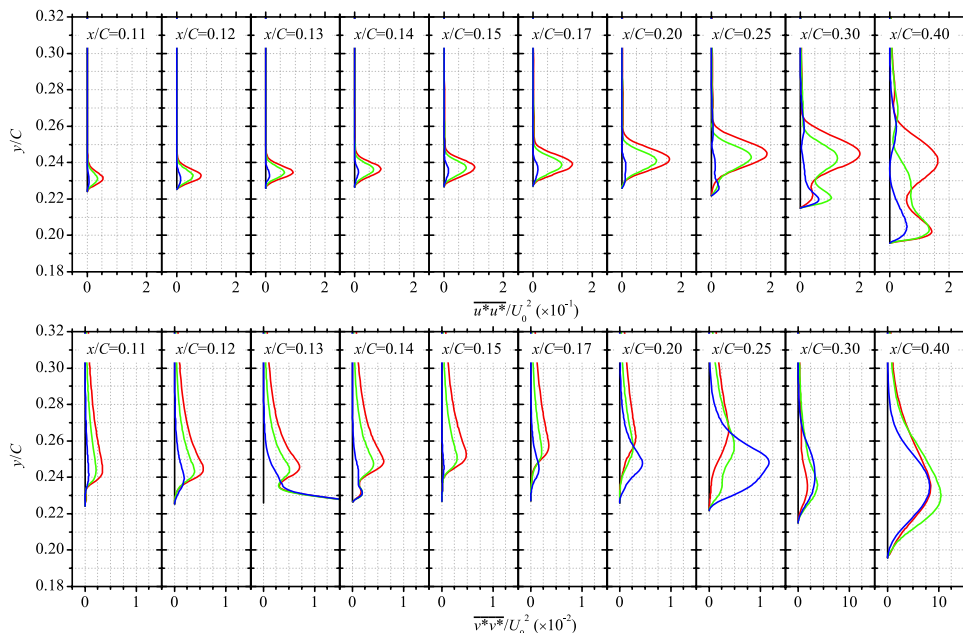

FIG. 15. Distributions of mean coherent Reynolds stresses $\overline{u^*u^*}/U_0^2$ and $\overline{v^*v^*}/U_0^2$ at several streamwise stations close to the actuator. Black curves for baseline; red curves for $F^+ = 0.5$; green curves for $F^+ = 1.0$; blue curves for $F^+ = 4.0$.

the LF case is larger than the MF and HF cases. The profiles of $\overline{u^*u^*}$ at $x/C = 0.30$ and 0.40 clearly show two maxima with one close to the wall and the other approximately in the shear layer, which are attributed to the periodic convection of the discrete vortices whose top and bottom sides roughly coincide with maxima in these regions. Similarly, the maximum value of $\overline{v^*v^*}$ is also induced by the periodic passing separated vortices but with only one peak appears approximately between the two maxima of corresponding $\overline{u^*u^*}$ due to the periodic upwash/downwash of the left/right side of the passing vortices, which is especially apparent at $x/C = 0.40$.

4. Effects on the upstream flow

In the present study, the peak blowing/suction velocity of the SJ is only 20% that of the cross-flow, and the momentum coefficient of the SJ is even smaller because of the Poiseuille-type velocity profile and the sinusoidally time-varying pattern. Moreover, since the actuator of the SJ is positioned at $x^+ = 0.13$ and the velocity is normal to the local surface, the velocity vector is $(u, v, w)_{\text{jet}}/U_0 = (\pm 0.064, \mp 0.997, 0.000)$ across the whole actuator exit. These numbers demonstrate that the SJ is only slightly pointing upstream and the streamwise component of the jet velocity is quite small considering the high kinetic energy of the cross-flow. However, the perturbation introduced by the SJ may be propagated by the pressure field, and we are interested in how much the flow field, both upstream and downstream of the actuator, is affected by the SJ and its amplified pattern. Figure 16 gives the streamwise distributions of the peak rms values of the spanwise-averaged coherent velocities. The peak coherent velocities are enhanced by the SJ compared with the baseline case with an increase of more than two orders of magnitude above the actuator. In the downstream region, the corresponding value of u^* only slightly varies, while there is an obvious decrease of $(v^*_{\text{rms}})_{\text{max}}$ in the near wake for the HF case since the flow is less locked to the perturbation and turbulent fluctuations grow. The flow upstream of the actuator is also significantly affected by the SJ by way of pressure propagation in the incompressible flow. The peak rms values of u^* and v^* for the baseline case are negligibly small with maximum values of around $0.1\% U_0$. Taking $(u^*_{\text{rms}})_{\text{max}} = 1\% U_0$ as a criterion, the flow field in the HF case is affected by the SJ to the most upstream position of $x/C = 0.03$, while in the LF and MF cases, it is affected up to a further position of around $x/C = -0.03$. The corresponding values of $(v^*_{\text{rms}})_{\text{max}}$ in the LF, MF, and HF cases are, respectively, around $x/C = -0.05, -0.02$, and 0.08. Considering the fact that the oncoming flow is steady and the turbulent fluctuation upstream of the actuator is almost zero (see Figure 9),
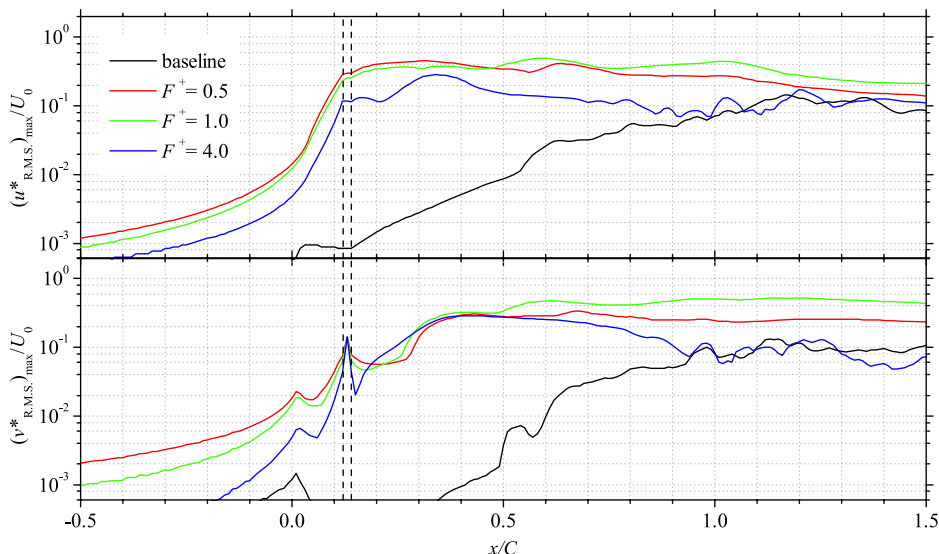

FIG. 16. Streamwise distributions of peak rms values of coherent velocity components. The dashed lines indicate the position of the actuator.

the fluctuations are entirely contributed by the SJ. In other words, the perturbation of the SJ could obviously affect the flow field up to 18%C upstream of the actuator centre as shown in the LF case, where the peak rms value of v^* is 1% of the uniform cross-flow velocity. Although the criterion of 1%U_0 is comparably much smaller than the peak values downstream of the actuator, the above analysis reveals that the SJ could also noticeably affect the upstream flow field within a certain distance.

IV. CONCLUSIONS

In this study, we presented results of direct numerical simulations on a synthetic jet based separation control of flow past a NACA-0018 airfoil, at 10° angle of attack and Reynolds number $Re_C = 10^4$. The SJ is simply modeled by a nominally 2D oscillatory velocity boundary condition on the airfoil leeward surface just upstream of the separation point of the uncontrolled flow, and its momentum coefficient is fixed at a small value $C_\mu = 2.13 \times 10^{-4}$. We focus on the effects of the forcing frequency of the SJ on the separation control, including the aerodynamic performance improvement, the temporal and spatial evolutions of the SJ induced coherent structures, and the lock-in of the flow on the forcing. The forcing frequency of the SJ is chosen at three values: the low frequency $F^+ = 0.5$, the medium frequency $F^+ = 1.0$, and the high frequency $F^+ = 4.0$.

The effects of the geometric variation introduced by the actuator of the SJ are first studied by conducting two simulations: the uncontrolled baseline case, and the zero-jet case in which the airfoil profile is modified by the actuator but no blowing/suction is applied. The results demonstrate that in the present configuration and parameter space, the separation control is attributed to the SJ while the effects of the geometric variation due to the actuator are negligible. The lift and lift-to-drag ratio of the airfoil are improved by the employment of the SJ at all three forcing frequencies. Separation is significantly reduced both in size and duration. The SJ operated at low and medium frequencies gives better improvement in that the large separation zone is reduced in the time-averaged sense, while the actuation at high frequency results in a large separation zone at the trailing edge.

Since the SJ provides extra perturbation to the flow, we are most interested in the temporal-spatial behavior of the unsteady flow subjected to the periodic forcing. Spectral analysis of the temporal variations of velocity at several probes reveals that the shear layer in the uncontrolled case has a broadband spectrum that may respond to perturbation in a wide frequency range. In the controlled cases, the flow in the shear layer is better locked to the forcing, while the flow in the separation zone and wake is less perfectly locked due to the growing turbulent fluctuations. The flow in the MF case is well organized in both the shear layer and wake since the forcing frequency $F^+ = 1.0$ is closest to the natural frequency f_{wake} of the uncontrolled flow. Based on the forcing frequency of the SJ, there are basically two modes of vortex dynamics downstream of the actuator: the *vortex fragmentation and merging mode* at low frequency in which the separation bubble formed due to the SJ breaks up into several vortices and they may merge as convecting downstream; the *discrete vortices mode* at high frequency that the separation bubble convects downstream without any breakup and merging, thus forming a set of discrete vortices. The convection velocity of the discrete vortices in the second mode is $0.5U_0$, which is close to the value in the configurations of a backward-facing step or ramp. The convection velocities in the LF and MF cases are close but are smaller than that of the HF case.

Since the direction of the jet velocity is normal to the local airfoil surface, the jet is slightly pointing upstream with a velocity vector $(u, v, w)_{\text{jet}}/U_0 = (-0.064, 0.997, 0.000)$. However, the jet affects not only the flow downstream of the actuator but also upstream of it. In the LF case where the momentum rate is the largest during the blowing phase, the SJ could increase the peak rms value of the coherent velocity to 1%U_0 as far as a position 18%C upstream of the actuator, which is a significant value considering the tiny momentum coefficient of the SJ.

In the present study, we only considered the SJ-based separation control of the incoming laminar flow past an airfoil, while in practice the incoming flow is likely to be turbulent in which case the control effects and related flow mechanisms must be revisited. The effectiveness of the SJ on separation control and improvement of aerodynamic performances has been experimentally

confirmed for the low-intensity turbulent incoming flow.[23] We believe that the turbulent flow would exhibit similar responses to the actuation and that similar vortex dynamical patterns be exhibited since the virtual aero-shaping effects can be maintained. Nevertheless, a more thorough investigations is warranted for an incoming turbulent flow to confirm the feasibility of the SJ in potential engineering applications. Such a study will be part of a future investigation.

ACKNOWLEDGMENTS

[1] P. B. S. Lissaman, "Low-Reynolds-number airfoils," Annu. Rev. Fluid Mech. **15**, 223–239 (1983).

[2] T. J. Mueller and J. D. DeLaurier, "Aerodynamics of small vehicles," Annu. Rev. Fluid Mech. **35**, 89–111 (2003).

[3] D. J. Pines and F. Bohorquez, "Challenges facing future micro-air-vehicle development," J. Aircr. **43**, 290–305 (2006).

[4] H. P. Horton, "Laminar separation bubbles in two and three dimensional incompressible flow," Ph.D. thesis, University of London, 1968.

[5] D. Greenblatt and I. J. Wygnanski, "The control of flow separation by periodic excitation," Prog. Aerosp. Sci. **36**, 487–545 (2000).

[6] G. Godard and M. Stanislas, "Control of a decelerating boundary layer. Part 1: Optimization of passive vortex generators," Aerosp. Sci. Technol. **10**, 181–191 (2006).

[7] L. Huang, P. G. Huang, R. P. LeBeau, and T. Hauser, "Numerical study of blowing and suction control mechanism on NACA0012 airfoil," J. Aircr. **41**, 1005–1013 (2004).

[8] T. L. Chng, A. Rachman, H. M. Tsai, and G.-C. Zha, "Flow control of an airfoil via injection and suction," J. Aircr. **46**, 291–300 (2009).

[9] N. O. Packard, M. P. Thake, Jr., C. H. Bonilla, K. Gompertz, and J. P. Bons, "Active control of flow separation on a laminar airfoil," AIAA J. **51**, 1032–1041 (2013).

[10] T. Suzuki, T. Colonius, and S. Pirozzoli, "Vortex shedding in a two-dimensional diffuser: Theory and simulation of separation control by periodic mass injection," J. Fluid Mech. **520**, 187–213 (2004).

[11] S. T. Deng, L. Jiang, and C. Q. Liu, "DNS for flow separation control around an airfoil by pulsed jets," Comput. Fluids **36**, 1040–1060 (2007).

[12] A. Gross and H. F. Fasel, "Active flow control for NACA 6-series airfoil at Re= 64,200," AIAA J. **48**, 1889–1902 (2010).

[13] D. Postl, W. Balzer, and H. F. Fasel, "Control of laminar separation using pulsed vortex generator jets: Direct numerical simulations," J. Fluid Mech. **676**, 81–109 (2011).

[14] A. Glezer and M. Amitay, "Synthetic jets," Annu. Rev. Fluid Mech. **34**, 503–529 (2002).

[15] M. Gad-el-Hak and D. M. Bushnell, "Separation control: Review," J. Fluids Eng. **113**, 5–30 (1991).

[16] P. F. Zhang, J. J. Wang, and L. H. Feng, "Review of zero-net-mass-flux jet and its application in separation flow control," Sci. China, Ser. E: Technol. Sci. **51**, 1315–1344 (2008).

[17] A. Avdis, S. Lardeau, and M. Leschziner, "Large eddy simulation of separated flow over a two-dimensional hump with and without control by means of a synthetic slot-jet," Flow, Turbul. Combust. **83**, 343–370 (2009).

[18] T. Suzuki, "Effects of a synthetic jet acting on a separated flow over a hump," J. Fluid Mech. **547**, 331–359 (2006).

[19] A. Naim, D. Greenblatt, A. Seifert, and I. Wygnanski, "Active control of a circular cylinder flow at transitional Reynolds numbers," Flow, Turbul. Combust. **78**, 383–407 (2007).

[20] J. Dandois, E. Garnier, and P. Sagaut, "Numerical simulation of active separation control by a synthetic jet," J. Fluid Mech. **574**, 25–58 (2007).

[21] M. Amitay, D. R. Smith, V. Kibens, D. E. arekh, and A. Glezer, "Aerodynamic flow control over an unconventional airfoil using synthetic jet actuators," AIAA J. **39**, 361–370 (2001).

[22] A. Seifert and L. G. Pack, "Compressibility and excitation location effects on high Reynolds numbers active separation control," J. Aircr. **40**, 110–119 (2003).

[23] N. A. Buchmann, C. Atkinson, and J. Soria, "Influence of ZNMF jet flow control on the spatio-temporal flow structure over a NACA-0015 airfoil," Exp. Fluids **54**, 1–14 (2013).

[24] R. Raju, R. Mittal, and L. Cattafesta, "Dynamics of airfoil separation control using zero-net mass-flux forcing," AIAA J. **46**, 3103–3115 (2008).

[25] R. B. Kotapati, R. Mittal, and L. N. Cattafesta III, "Numerical experiments in synthetic jet based separation control," AIAA Paper 2006-0320, 2006.

[26] E. Chatlynne, N. Rumigny, M. Amitay, and A. Glezer, "Virtual aero-shaping of a Clark-Y airfoil using synthetic jet actuators," AIAA Paper 2001-0732, 2001.

[27] R. Mittal and P. Rampunggoon, "On the virtual aeroshaping effect of synthetic jets," Phys. Fluids **14**, 1533–1536 (2002).

[28] G. Godard, J.-M. Foucaut, and M. Stanislas, "Control of a decelerating boundary layer. Part 2: Optimization of slotted jets vortex generators," Aerosp. Sci. Technol. **10**, 394–400 (2006).

[29] G. Godard and M. Stanislas, "Control of a decelerating boundary layer. Part 3: Optimization of round jets vortex generators," Aerosp. Sci. Technol. **10**, 455–464 (2006).

[30] O. Sahni, J. Wood, K. E. Jansen, and M. Amitay, "Three-dimensional interactions between a finite-span synthetic jet and a crossflow," J. Fluid Mech. **671**, 254–287 (2011).

[31] J. Z. Wu, X. Y. Lu, A. G. Denny, M. Fan, and J. M. Wu, "Post-stall flow control on an airfoil by local unsteady forcing," J. Fluid Mech. **371**, 21–58 (1998).

[32] R. Duvigneau and M. Visonneau, "Optimization of a synthetic jet actuator for aerodynamic stall control," Comput. Fluids **35**, 624–638 (2006).

[33] R. B. Kotapati, R. Mittal, O. Marxen, F. Ham, D. You, and L. N. Cattafesta, "Nonlinear dynamics and synthetic-jet-based control of a canonical separated flow," J. Fluid Mech. **654**, 65–97 (2010).

[34] A. Seifert and L. G. Pack, "Oscillatory control of separation at high Reynolds numbers," AIAA J. **37**, 1062–1071 (1999).

[35] A. Glezer, M. Amitay, and A. M. Honohan, "Aspects of low-and high-frequency actuation for aerodynamic flow control," AIAA J. **43**, 1501–1511 (2005).

[36] G. B. McCullough and D. E. Gault, "Examples of three representative types of airfoil-section stall at low speed," Technical Report, TN-2502, NACA, 1951.

[37] P. K. Chang, *Control of Flow Separation* (McGraw-Hill, 1976).

[38] D. You and P. Moin, "Active control of flow separation over an airfoil using synthetic jets," J. Fluids Struct. **24**, 1349–1357 (2008).

[39] A. Tuck and J. Soria, "Separation control on a NACA 0015 airfoil using a 2D micro ZNMF jet," Aircr. Eng. Aerosp. Technol. **80**, 175–180 (2008).

[40] L. E. Jones, R. D. Sandberg, and N. D. Sandham, "Direct numerical simulations of forced and unforced separation bubbles on an airfoil at incidence," J. Fluid Mech. **602**, 175–207 (2008).

[41] Y. Hoarau, M. Braza, Y. Ventikos, D. Faghani, and G. Tzabiras, "Organized modes and the three-dimensional transition to turbulence in the incompressible flow around a NACA0012 wing," J. Fluid Mech. **496**, 63–72 (2003).

[42] V. Kitsios, L. Cordier, J. P. Bonnet, A. Ooi, and J. Soria, "On the coherent structures and stability properties of a leading-edge separated aerofoil with turbulent recirculation," J. Fluid Mech. **683**, 395–416 (2011).

[43] J. Fröhlich, C. P. Mellen, W. Rodi, L. Temmerman, and M. A. Leschziner, "Highly resolved large-eddy simulation of separated flow in a channel with streamwise periodic constrictions," J. Fluid Mech. **526**, 19–66 (2005).

[44] Y. Morinishi, T. S. Lund, O. V. Vasilyev, and P. Moin, "Fully conservative higher order finite difference schemes for incompressible flow," J. Comput. Phys. **143**, 90–124 (1998).

[45] T. A. Zang, "On the rotation and skew-symmetric forms for incompressible flow simulations," Appl. Numer. Math. **7**, 27–40 (1991).

[46] Y. Zang, R. L. Street, and J. R. Koseff, "A non-staggered grid, fractional step method for time-dependent incompressible Navier–Stokes equations in curvilinear coordinates," J. Comput. Phys. **114**, 18–33 (1994).

[47] W. C. Reynolds and A. K. M. F. Hussain, "The mechanics of an organized wave in turbulent shear flow. Part 3. Theoretical models and comparisons with experiments," J. Fluid Mech. **54**, 263–288 (1972).

[48] B. Cantwell and D. Coles, "An experimental study of entrainment and transport in the turbulent near wake of a circular cylinder," J. Fluid Mech. **136**, 321–374 (1983).

[49] D. A. Lyn, S. Einav, W. Rodi, and J. H. Park, "A laser-doppler velocimetry study of ensemble-averaged characteristics of the turbulent near wake of a square cylinder," J. Fluid Mech. **304**, 285–319 (1995).

[50] M. Hayakawa and F. Hussain, "Three-dimensionality of organized structures in a plane turbulent wake," J. Fluid Mech. **206**, 375–404 (1989).

[51] S. Balachandar, R. Mittal, and F. M. Najjar, "Properties of the mean recirculation region in the wakes of two-dimensional bluff bodies," J. Fluid Mech. **351**, 167–199 (1997).

[52] M. Breuer and N. Jovičić, "Separated flow around a flat plate at high incidence: An LES investigation," J. Turbul. **2**, 1–15 (2001).

[53] R. Holman, Y. Utturkar, R. Mittal, B. L. Smith, and L. Cattafesta, "Formation criterion for synthetic jets," AIAA J. **43**, 2110–2116 (2005).

[54] E. Lamballais, J. Silvestrini, and S. Laizet, "Direct numerical simulation of flow separation behind a rounded leading edge: Study of curvature effects," Int. J. Heat Fluid Flow **31**, 295–306 (2010).